Structural and magnetic field effects on spin fluctuations in $Sr_3Ru_2O_7$

Shantanu Mukherjee* and Wei-Cheng Lee†

Department of Physics, Applied Physics, and Astronomy, Binghamton University–State University of New York, Binghamton, New York 13902, USA

(Received 4 April 2016; revised manuscript received 21 July 2016; published 5 August 2016)

We investigate the evolution of magnetic excitations in $Sr_3Ru_2O_7$ in the paramagnetic metallic phase using a three-band tight-binding model. The effect of Mn or Ti dopant ions on the $Sr_3Ru_2O_7$ band structure has been included by taking into account the dopant-induced suppression of the oxygen octahedral rotation in the tight-binding band structure. We find that the low-energy spin fluctuations are dominated by three wave vectors around $\vec{q} = ((0,0),(\pi/2,\pi/2))$ and $(\pi,0)$, which compete with each other. As the octahedral rotation is suppressed with increasing doping, the three wave vectors evolve differently. In particular, the undoped compound has dominant wave vectors at $\vec{q} = ((0,0),(\pi/2,\pi/2))$, but doping $Sr_3Ru_2O_7$ leads to a significant enhancement in the spin susceptibility at the $\vec{q} = (\pi,0)$ wave vector, bringing the system closer to a magnetic instability. All the features calculated from our model are in agreement with neutron scattering experiments. We have also studied the effect of a c-axis Zeeman field on the low-energy spin fluctuations. We find that an increasing magnetic field suppresses the antiferromagnetic (AFM) fluctuations and leads to stronger competition between the AFM and ferromagnetic spin fluctuations. The magnetic field dependence observed in our calculations therefore supports the scenario that the observed nematic phase in the metamagnetic region in $Sr_3Ru_2O_7$ is intimately related to the presence of a competing ferromagnetic instability.

DOI: 10.1103/PhysRevB.94.064407

I. INTRODUCTION

The bilayer compound $Sr_3Ru_2O_7$ (Sr327) is a member of the Ruddlesden-Popper series [1]. Although it is not superconducting like single-layer Sr_2RuO_4 [2], the phase diagram of $Sr_3Ru_2O_7$ is quite rich. The undoped compound is a metamagnetic metal on the verge of ferromagnetism and shows a region of significant change in resistivity [3–5] and development of a spin-density wave order in moderate magnetic fields ($B \sim 8$ T magnetic field applied along the c axis) [6]. Rotating the field direction away from the c axis affects the metamagnetic transition, and a nematic state has been observed that is characterized by a strong anisotropy in resistivity within the ab plane [6,7]. Apart from the unusual magnetic field behavior, doping $Sr_3Ru_2O_7$ with Mn or Ti also leads to a number of interesting properties. Both Mn and Ti act as substitutional impurities and replace the Ru ions. Above a critical doping concentration of $x \sim 5\%$, lowering the temperature leads to an insulating state followed by a long-range antiferromagnetic order [8,9]. The metal-insulator transition temperature grows with doping, whereas the long-range antiferromagnetic (AFM) state shows a domelike behavior in the temperature-doping phase diagram and exists up to a doping level of $x \sim 20\%$ [8,10,11]. Small amounts of Ti dopants in Sr327 suppress the metamagnetic transition, and this suppression has been argued to result from competing magnetic interactions in Sr327 [12]. Therefore understanding the low-energy spin fluctuations in Mn- or Ti-doped Sr327 compounds will be crucial for unraveling the origin of dopant-induced magnetic order as well as the physics of metamagnetic transition.

Undoped Sr327 is nonmagnetic but shows low-energy spin fluctuations at the $\vec{q}_{AFM} = (q_x,q_y) = (\pi/2,\pi/2)$ wave vector [13]. Note that the $\vec{q}$ vector has been expressed here in the smaller orthorhombic Brillouin zone [see Fig. 1(b)]. Inelastic neutron scattering experiments also observe enhanced incommensurate ferromagnetic spin fluctuations at $\vec{q}_{FM} \sim (0.09,0.09,0)$ [13]. These features in the paramagnetic undoped compound can be understood from general Fermi-surface nesting arguments [14]. However, upon doping with Mn, neutron scattering experiments find a long-range AFM state [15] with a dominant wave vector at $\vec{q} \sim (\pi,0)$, and doping with isovalent Ti^{4+} ions leads to an AFM state with the incommensurate wave vector $\vec{q} \sim (\pi + \delta,0)$ [11]. Therefore this strong shift in the ordering vector of low-energy fluctuations cannot be explained simply by a rigid band shift induced by Mn doping. It is not well understood if the significant shift in direction and magnitude of the $\vec{q}$ vector with Mn or Ti doping is due to a change in the nesting properties of the Fermi surface caused by structural effects of doping or whether we need to consider the physics of the insulating phase to understand the formation of long-range antiferromagnetic order. In the former scenario we can expect that the essential ingredients of spin-correlation physics leading to a shift in $\vec{q}$ with doping would already be present in the high-temperature metallic phase.

Structurally, the $Sr_3Ru_2O_7$ compound differs from Sr_2RuO_4 not only by the presence of a bilayer coupling but also by a significant oxygen octahedral rotation of $\theta \sim 7^\circ$ [16]. The band folding associated with the rotated octahedra leads to a complex Fermi surface and band structure in $Sr_3Ru_2O_7$ [17]. The structural parameter controlling the degree of octahedral rotation is strongly affected by the presence of Mn dopants. It has been observed in x-ray diffraction experiments that upon increasing the Mn concentration, the octahedral rotation is suppressed by a doping of $x \sim 16\%$ [18,19]. Therefore in order to identify the mechanism governing the magnetic order

*smukherj@binghamton.edu
†wlee@binghamton.edu

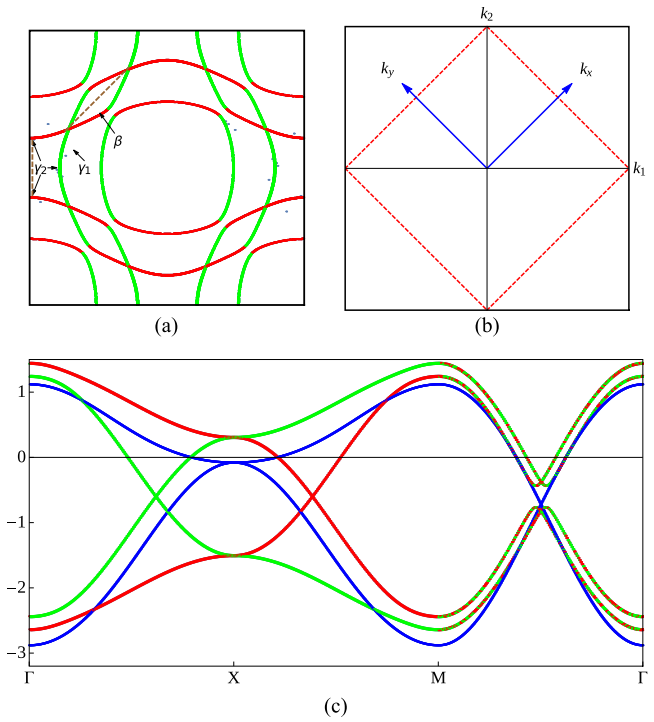

FIG. 1. (a) The Fermi surface for $x \sim 1\%$ in the tetragonal unit cell. The colors represent the dominant orbital content with d_{yz} (red), d_{xz} (green), and d_{xy} (blue). The dashed brown lines represent the dominant $(\pi,0)$ nesting on the β pocket observed in the doped compound and the dominant $(\pi/2,\pi/2)$ nesting on the γ_2 pocket observed in the undoped compound. (b) The larger tetragonal zone (k_1,k_2) (black) and smaller orthorhombic Brillouin zone (k_x,k_y) (dashed red lines). (c) The band structure along high-symmetry directions in the tetragonal unit cell showing the position of the Van Hove singularity near the X point.

we need to study the effects of changes in octahedral rotation on the low-energy spin fluctuations.

In this work, we use a three-orbital tight-binding model with spin-orbit interaction and octahedral rotation applicable to Sr327 and calculate the dynamical spin susceptibility $\chi(\vec{q},\omega)$ in the high-temperature metallic phase. Electron correlations are introduced using a multiorbital Hubbard-Hund Hamiltonian, and interacting susceptibility is calculated within a random-phase approximation (RPA). A similar tight-binding model has been used to study the nematic order in undoped Sr327 compounds [20,21]. We simulate the doping dependence of the octahedral rotation on this system by the suppression of a single tight-binding hopping parameter that accounts for the effect of Mn doping on the octahedral rotation. We find that the imaginary part of spin susceptibility indeed shifts from $\vec{q} \sim (\pi/2,\pi/2)$ in the undoped compound to $\vec{q} \sim (\pi,0)$ near optimal doping. Additionally, the spin fluctuations are strongly enhanced in magnitude as octahedral rotation gets suppressed, indicating a tendency towards a magnetic order at the $\vec{q} \sim (\pi,0)$ wave vector observed in experiments. This provides evidence that the magnetic transition in Mn-doped $Sr_3Ru_2O_7$ is primarily governed by the doping induced changes in the lattice structure. We further calculate the effect of a c-axis Zeeman field on the spin fluctuations in the undoped compound which is relevant to high-temperature paramagnetic phase where the nematic fluctuations can be neglected. We find that the AFM fluctuations not only become more incommensurate but also get progressively weaker near the $\vec{q} \sim (\pi/2,\pi/2)$ region. The calculated suppression of spin susceptibility with magnetic field in the high-temperature paramagnetic phase indicates that the observation of a spin-density-wave (SDW) transition in finite magnetic fields cannot be understood from the bare Hamiltonian and requires the inclusion of additional effects such as nematic ordering that has been proposed to exist in the low-temperature phase of undoped Sr327 [20,21]. However, we do find that the presence of a c-axis magnetic field in the high-temperature phase leads to a stronger competition between the AFM and ferromagnetic (FM) fluctuations in the undoped Sr327 compound, and the spin fluctuations shift from the $(\pi/2,\pi/2)$ position towards the incommensurate wave vector that has been observed for the SDW phase in a finite magnetic field.

II. MODEL

Tight-binding Hamiltonian. The electronic structure of $Sr_3Ru_2O_7$ has been modeled using a three-orbital tight-binding model consisting of the t_{2g} orbitals (d_{xz},d_{yz},d_{xy}) which are most relevant for their low-energy properties [20,22]. The tight-binding model has been argued to reproduce the essential features of the electronic structure of the Sr327 compound and has been used to analyze the physics of the nematic state near the metamagnetic transition [20] and model the quasiparticle interference patterns [22]. The Hamiltonian is given by

$$H = H_0 + H_{\mathrm{INT}}. \tag{1}$$

The tight-binding Hamiltonian H_0 for the Sr327 compound can be written as a 12×12 matrix. This includes the enlarged unit cell due to the effect of oxygen octahedral rotation that leads to two sublattices which can be expressed in momentum space by the characteristic wave vector $\vec{Q} = (\pi,\pi)$ in the tetragonal basis. The unit cell is further enlarged along the c axis due to the splitting of electronic bands by a bilayer interaction. As discussed in Ref. [22], the Hamiltonian can be decoupled into two independent parts after Fourier transforming along the layer index. Therefore, writing the bilayer Hamiltonian as $H_0 = h_0(k_z = 0) + h_0(k_z = \pi)$, each component is given by

$$h_0(k_z) = \sum_{\vec{k}} \Phi^{\dagger}_{\vec{k},s,k_z} \begin{pmatrix} \hat{h}_{0s}(\vec{k},k_z) & \hat{g}^{\dagger}(\vec{k},k_z) \\ \hat{g}(\vec{k},k_z) & \hat{h}_{0s}(\vec{k}+\vec{Q},k_z) \end{pmatrix} \Phi_{\vec{k},s,k_z}, \tag{2}$$

where

$$\Phi_{\vec{k},s,k_z} = \left(d^{yz}_{\vec{k},s,k_z}, d^{xz}_{\vec{k},s,k_z}, d^{xy}_{\vec{k},-s,k_z}, d^{yz}_{\vec{k}',s,k_z}, d^{xz}_{\vec{k}',s,k_z}, d^{xy}_{\vec{k}',-s,k_z}\right), \tag{3}$$

with $\vec{k}' = \vec{k} + \vec{Q}$, and $d^{\alpha}_{\vec{k},s,k_z}$ annihilates an electron with orbital α, spin s, in-plane momenta $\vec{k}$, and momentum along the z direction k_z. The matrix components are given by

$$\hat{h}_{0s}(\vec{k},k_z) = \hat{A}_s(\vec{k}) + \hat{B}_1 \cos(k_z), \tag{4}$$

$$\hat{g}(\vec{k},k_z) = \hat{G}(\vec{k}) - 2\hat{B}_2 \cos(k_z). \tag{5}$$

The 3×3 matrix kernels are the intralayer hopping contribution without octahedral rotation $\hat{A}_s(\vec{k})$, staggered in-plane hopping $\hat{G}(\vec{k})$, interlayer hopping without rotation $\hat{B}_1$, and staggered interlayer hopping $\hat{B}_2$. These hopping matrix elements have been derived in Ref. [22] and are given by

$$\hat{A}_s(\vec{k}) = \begin{pmatrix} \epsilon_{\vec{k}}^{yz} & \epsilon_{\vec{k}}^{\text{off}} + is\lambda & 0 \\ \epsilon_{\vec{k}}^{\text{off}} - is\lambda & \epsilon_{\vec{k}}^{xz} & 0 \\ 0 & 0 & \epsilon_{\vec{k}}^{xy} \end{pmatrix}, \tag{6}$$

$$\hat{G}(\vec{k}) = \begin{pmatrix} 0 & t_{\text{rot}}\gamma_{\vec{k}} & 0 \\ -t_{\text{rot}}\gamma_{\vec{k}} & 0 & 0 \\ 0 & 0 & 0 \end{pmatrix}, \tag{7}$$

$$\hat{B}_1 = \begin{pmatrix} -t_\perp & 0 & 0 \\ 0 & -t_\perp & 0 \\ 0 & 0 & 0 \end{pmatrix}, \tag{8}$$

$$\hat{B}_2 = \begin{pmatrix} 0 & t_{\text{INT}}^\perp & 0 \\ -t_{\text{INT}}^\perp & 0 & 0 \\ 0 & 0 & 0 \end{pmatrix}. \tag{9}$$

In the above equations, the single-particle energies are given by

$$\epsilon_{\vec{k}}^{xz} = -2t_1\cos(k_1) - 2t_2\cos(k_2), \tag{10}$$

$$\epsilon_{\vec{k}}^{yz} = -2t_2\cos(k_1) - 2t_1\cos(k_2), \tag{11}$$

$$\epsilon_{\vec{k}}^{xy} = -2t_3[\cos(k_1) + \cos(k_2)] - 4t_4\cos(k_1)\cos(k_2) - 2t_5[\cos(2k_1) + \cos(2k_2)], \tag{12}$$

$$\epsilon_{\vec{k}}^{\text{off}} = -4t_6\sin(k_1)\sin(k_2). \tag{13}$$

The above tight-binding Hamiltonian is given in the tetragonal basis (k_1,k_2) and can be converted to the basis of the smaller octahedral Brillouin zone (k_x,k_y) with the transformation $k_x = k_1 + k_2$, $k_y = k_2 - k_1$. The hopping matrix elements are in units of $t \sim 300$ meV, with $t_1 = t_3 = 0.5$, $t_2 = 0.05$, $t_4 = 0.1$, $t_5 = -0.03$, and $t_6 = 0.05$. The spin-orbit coupling coefficient is given by $\lambda = 0.1$. The spin-orbit coupling λ is assumed to primarily couple the $d_{xz/yz}$ orbitals and ignores the coupling to the d_{xy} orbital. A similar spin-orbit coupling term has been argued to explain the low-energy fluctuations in Sr_2RuO_4 [23].

The staggered in-plane hopping contains the hopping term t_{rot}, and $\gamma_{\vec{k}} = \cos(k_1) + \cos(k_2)$. This term primarily describes the effect of intraplane hopping induced by staggered rotation of octahedral oxygen and includes the leading effect on the hopping between nearest-neighbor Ru sites in Sr327 [22]. The suppression of octahedral rotation with Mn doping can be simulated by a reduction in t_{rot} that characterizes the strength of octahedral rotation in real space and governs the extent of hybridization due to band folding in reciprocal space. We therefore use the octahedral rotation hopping matrix element t_{rot} as a free parameter to study the doping dependence of low-energy spin fluctuations on the Sr327 compound. Although we also include a weak bilayer splitting of the bands by including finite $t_\perp = 0.005$ and $t_{\text{INT}}^\perp = 0.005$ hopping terms, they have been kept fixed as a function of doping. This is reasonable since the bilayer terms do not have a significant effect on the doping dependence of the low-energy spin fluctuations.

Zeeman field. We study the effect of an external magnetic field oriented along the out-of-plane c-axis direction. The magnetic field couples to both spin and orbital degrees of freedom and modifies the electronic structure. For an arbitrary magnetic field direction it is given by

$$H_B = -\mu_B\vec{B}_i \cdot \sum_i (\vec{L}_i + 2\vec{S}_i); \tag{14}$$

this leads to the following form for a field along the c-axis direction:

$$H_{\text{Zeeman}} = -i\mu_B B_z \sum_{s,\vec{k}} \left(d_{\vec{k},s}^{yz\dagger} d_{\vec{k},s}^{xz} - d_{\vec{k},s}^{xz\dagger} d_{\vec{k},s}^{yz}\right) - \frac{g\mu_B B_z}{2} \sum_{\vec{k},\alpha} \left(d_{\vec{k}\uparrow}^{\alpha\dagger} d_{\vec{k}\uparrow}^{\alpha} - d_{\vec{k}\downarrow}^{\alpha\dagger} d_{\vec{k}\downarrow}^{\alpha}\right). \tag{15}$$

Here the energy scale for the Zeeman term B is expressed in units of hopping t. The first (second) sum corresponds to the orbital (spin) contribution to the Zeeman term.

Hubbard-Hund Hamiltonian. The electron correlations are included in our model using an on-site Hubbard-Hund Hamiltonian. Following the discussion in Ref. [24], the interaction Hamiltonian is approximated to have a spherical symmetry and in real space can be written as

$$H_{\text{INT}} = \sum_{i\mu\nu\theta\psi s_1 s_2} U_{\theta\psi s_2}^{\mu\nu s_1} d_{i\mu s_1}^\dagger d_{i\nu s_1} d_{i\theta s_2}^\dagger d_{i\psi s_2}, \tag{16}$$

where i is the site index, (μ,ν,θ,ψ) represent the d- orbital indices, and s_1,s_2 are the spin indices. The components of the interaction matrix are given in Ref. [24] and also reproduced in the Appendix.

Spin susceptibility. For a multiorbital system the bare dynamical susceptibility is a tensor. In the presence of a spin-orbit coupling we need to calculate the tensor separately for the transverse and longitudinal directions. For the spin-up channel it can be expressed as

$$\chi_{l_1 l_2 l_3 l_4}^{\uparrow\uparrow}(\vec{q},i\omega_n) = \frac{1}{N}\sum_{\vec{k}\alpha\beta} W_{l_4 l_1 l_2 l_3}^{\alpha\beta}(\vec{k},\vec{q}) \frac{n_F\left(\epsilon_{\vec{k}+\vec{q}}^{\beta}\right) - n_F\left(\epsilon_{\vec{k}}^{\alpha}\right)}{i\omega_n + \left(\epsilon_{\vec{k}}^{\alpha} - \xi_{\vec{k}+\vec{q}}^{\beta}\right)}, \tag{17}$$

$$W_{l_4 l_1 l_2 l_3}^{\alpha\beta}(\vec{k},\vec{q}) = \psi_{l_4\uparrow}^{\alpha}(\vec{k})\psi_{l_1\uparrow}^{\alpha *}(\vec{k})\psi_{l_2\uparrow}^{\beta}(\vec{k}+\vec{q})\psi_{l_3\uparrow}^{\beta *}(\vec{k}+\vec{q}). \tag{18}$$

In the above (l_1,l_2,l_3,l_4) and (α,β) are orbital and band indices, respectively, ω_n are the Matsubara frequencies, $\psi_{l\sigma}^{\alpha}(\vec{k})$ and $\epsilon_{\vec{k}}^{\alpha}$ are the components of the eigenvectors and eigenvalues obtained by diagonalizing the tight-binding Hamiltonian, and $\vec{q}$ is the characteristic wave vector at which the spin susceptibility is calculated. Note that in the calculations performed in this work the vector $\vec{q}$ is expressed in the smaller orthorhombic Brillouin zone [see Fig. 1(b)]. The function $n_F(\epsilon_{\vec{k}}^{\beta})$ represents the Fermi function calculated at band energy $\epsilon_{\vec{k}}^{\beta}$. In the absence of a Zeeman field the calculation of other components of the bare susceptibility can be simplified using

the following symmetries:

$$\chi^{\downarrow\downarrow}_{l_1l_2l_3l_4}(\vec{q},i\omega_n) = \chi^{\uparrow\uparrow}_{l_4l_3l_2l_1}(\vec{q},i\omega_n), \quad (19)$$

$$\chi^{\uparrow\downarrow}_{l_1l_2l_3l_4}(\vec{q},i\omega_n) = \chi^{\uparrow\uparrow}_{l_4l_2l_3l_1}(\vec{q},i\omega_n). \quad (20)$$

We further include electron correlations in the susceptibility calculation using a RPA-based approach. We follow the formalism derived in Ref. [24] and provide the susceptibility expressions in the Appendix.

III. RESULTS

The Fermi surface of the 1% Mn-doped Sr327 compound obtained from our tight-binding model is shown in Fig. 1(a). This model reproduces well the observed Fermi surface sheets seen in angle-resolved photoemission spectroscopy (ARPES) experiments [20]. The small γ_2 pockets shown in Fig. 1(a) near the X-point [$(\pm\pi,0)$ and $(0,\pm\pi)$] regions of the tetragonal Brillouin zone have a dominant d_{xy} character on the curved sides and a $d_{xz/yz}$ character on the flatter sides. The γ_2 pocket in Fig. 1(a) has a crossing point with the γ_1 Fermi pocket. In general ARPES finds a hybridization between the γ_1 and γ_2 pockets due to an additional spin-orbit contribution $L_xS_x + L_yS_y$ which has been neglected in our study. This is justified because the additional spin-orbit contribution does not have a qualitative effect on our spin-susceptibility calculations since nesting primarily depends on the flatter regions of the Fermi surface and hence is not affected by the crossing points between different bands. Further note that the model does not include the inner Γ centered hole pocket which likely results from the e_g orbitals.

The most notable structural effect of Mn doping is the suppression of octahedral rotation [18]. The effect of Mn doping in $Sr_3(Ru_{1-x}Mn_x)_2O_7$ is considered by the variation of the hopping parameter $t_{\rm rot}$ that represents the influence of octahedral rotation on the tight-binding Hamiltonian; $t_{\rm rot} \sim 0.4$ ($t_{\rm rot} \sim 0.2$) leads to an electron doping of $n \sim 4.01e^-$/Ru ($4.15e^-$/Ru) with $x \propto n$ for an Mn-dopant ion. This range of doping x correctly corresponds to the region where the long-range antiferromagnetic order is observed at low temperatures. We discuss later the effect of an isovalent dopant such as Ti on the spin fluctuations in the higher-temperature metallic phase.

The calculated dynamical susceptibility in the longitudinal channel $\chi^{''}_{RPA}(\vec{q},\omega)$ is presented in Fig. 2. In Fig. 2(a) we show $\chi''_{RPA}(\vec{q},\omega)$ for $t_{\rm rot} = 0.4$ and an Mn doping of $x \sim 1\%$. The dominant low-energy spin fluctuations are peaked at the $\vec{q} = (\pi/2,\pi/2)$ wave vector, in agreement with neutron scattering experiments [13]. As can be seen from Fig. 2(c), the spin fluctuations in the undoped compound have a large contribution at $\vec{q} = (\pi/2,\pi/2)$ from the intraorbital susceptibility corresponding to the d_{xy} orbitals. The dominant d_{xy} orbital susceptibility contribution is due to a large density of states near the Fermi energy residing on the d_{xy}-orbital-dominated γ_2 Fermi pocket near the X points of the Brillouin zone. This pocket is progressively shifted away from the Fermi surface as $t_{\rm rot}$ decreases with Mn doping. Note that for the $x \sim 1\%$ compound in Fig. 2, there is a significant subdominant contribution to the susceptibility at $\vec{q} = (\pi,0)$ which can also be seen in the static spin susceptibility $\chi'(\vec{q},0)$ shown in

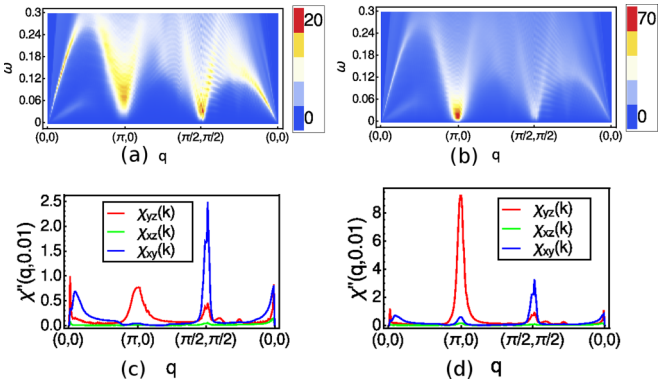

FIG. 2. Plots showing the imaginary part of RPA spin susceptibility $\chi''_{RPA}(\vec{q},\omega)$ for (a) $x = 1\%$ and (b) $x = 6\%$ Mn doping. The corresponding orbital-resolved spin-fluctuation components $\chi^{zz}_{aaaa}(\vec{q},0.01)$, where $a = (d_{yz},d_{xz},d_{xy})$ orbitals are shown for (c) $x = 1\%$ and (d) $x = 6\%$ doping. They have been calculated for $U = 0.8$ and $J = 0.25U$ and $k_BT = 0.007$.

Fig. 3(a). However, being weaker than the susceptibility at $\vec{q} = (\pi/2,\pi/2)$, it is relatively suppressed for a larger Coulomb interaction closer to the Stoner instability. In addition to the AFM fluctuations we also find strong but subdominant ferromagnetic spin fluctuations at low energies which disperse at higher energies. Interestingly, the relative strength of the AFM and FM fluctuations depends on the strength of the Coulomb interactions. We find that at low energies the FM fluctuations dominate in the imaginary part of the bare susceptibility but are weaker than AFM fluctuations for larger electron correlations.

In Fig. 2(b) we show the calculated $\chi''(\vec{q},\omega)$ for a weaker octahedral rotation $t_{\rm rot} = 0.36$ which corresponds to a doping of $x \sim 6\%$. The suppression of octahedral rotation not only shifts the spin fluctuations from $\vec{q} = (\pi/2,\pi/2)$ towards $\vec{q} = (\pi,0)$ but also enhances them significantly. This is evident from the doping dependence of $\chi'(\vec{q},0)$ plotted in Fig. 3(a), which shows that as the octahedral rotation gets reduced, there is a crossover from $\vec{q} = (\pi/2,\pi/2)$ to $\vec{q} = (\pi,0)$ in the susceptibility at $t_{\rm rot} \sim 0.355$ or $x \sim 5\%$. As can be seen from Fig. 2(d), the peak at $\vec{q} = (\pi,0)$ in doped Sr327 is primarily due to the $d_{xz/yz}$ intraorbital nesting channel on the β band,

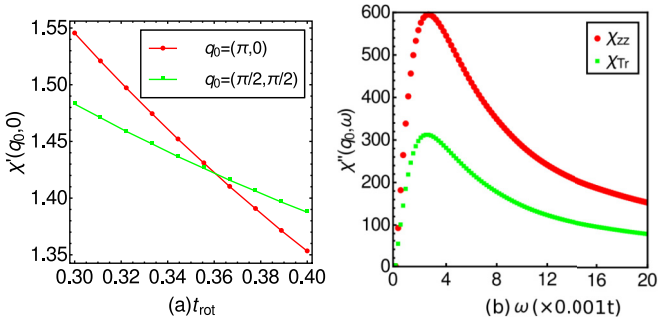

FIG. 3. (a) The Real part of spin susceptibility at $\vec{q} = (\pi,0)$ and $(\pi/2,\pi/2)$ as a function of increasing $t_{\rm rot}$ (or decrease in doping x). (b) The imaginary part for longitudinal and transverse susceptibilities at $x = 1\%$ doping and $\vec{q} = (\pi/2,\pi/2)$ as a function of energy.

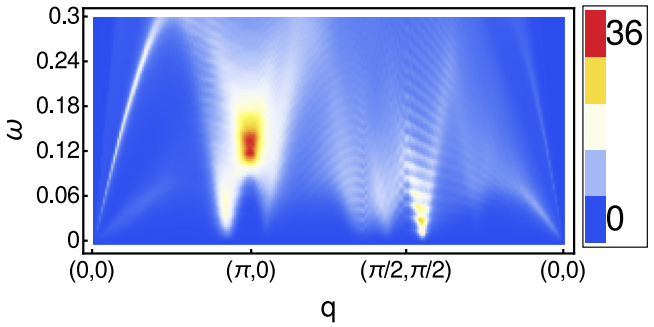

FIG. 4. Imaginary part of spin susceptibility $\chi''_{RPA}(\vec{q},\omega)$ for $t_{\rm rot} = 0.36$ and isovalent dopant showing development of incommensurate spin fluctuations.

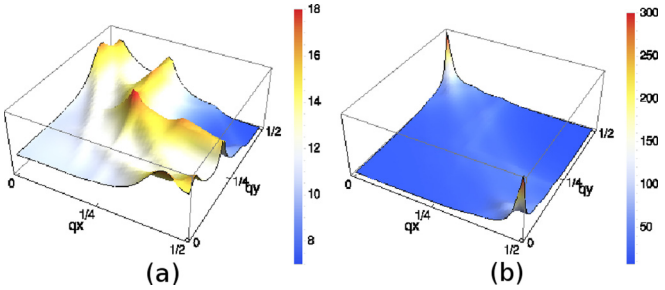

FIG. 5. The real part of susceptibility $\chi'_{RPA}(\vec{q},0)$ for $U = 0.8$, $J = 0.25U$. The q vector is represented in units of $2\pi t$. The plots correspond to (a) $x \sim 1\%$ and (b) $x \sim 6\%$.

unlike the undoped compound where the dominant fluctuations correspond to the d_{xy}-type γ_2 bands. Note that if the electron doping is kept fixed at $n = 4.01e^-$/Ru, as would be the case if the dopant ions act as isovalent Ti^{4+} ions, then as shown in Fig. 4, at $t_{\rm rot} = 0.36$ we find that the spin fluctuations are still enhanced but are shifted from the $\vec{q} = (\pi/2,0)$ point. This result is relevant to observations of the incommensurate wave vector seen in neutron experiments on Ti-doped Sr327 [11].

The enhancement in the susceptibility would bring the system close to a Stoner instability as the octahedral rotation gets progressively reduced with doping. Note that under this scenario local magnetic order can be expected to form near Mn dopants before the overall system crosses the Stoner instability. Such behavior has been observed in resonant elastic x-ray scattering experiment [9]. We therefore argue that the $\vec{q} = (\pi,0)$ magnetic state observed in Mn-doped Sr327 compounds is caused by a doping-induced structural distortion that leads to a change in nesting properties at the Fermi surface. These dominant spin fluctuations are already present in the high-temperature metallic phase.

In Fig. 3(b) we show the energy dependence of the dynamical susceptibility for the undoped system along the longitudinal and transverse directions. This anisotropy in the spin channel is caused by spin-orbit coupling and leads to an enhancement in the longitudinal bare susceptibility by a factor of 2, which has been argued to be the result of a larger number of scattering channels along the longitudinal direction [23]. The energy dependence shows a peak at $\omega \sim 1.5$ meV similar to the observation of a low-energy peak in inelastic neutron scattering experiments [13]. Such a peak at low energies in itinerant models usually indicates the proximity of the system to a Stoner instability and would not exist if the system is far from a magnetic instability.

The real part of the magnetic susceptibility $\chi'(\vec{q},0)$ is shown in Fig. 5(a) [Fig. 5(b)] for $x \sim 1\%$ ($x \sim 6\%$). Note that for the lower doping, in addition to the $\vec{q} = (\pi/2,\pi/2)$ peak in the susceptibility, there is significant weight around the $(\pi,0)$ regions and along the $(\pi/2,\pi/2) - (\pi/2,0)$ line. These pseudo-one-dimensional nesting regions are dominated by the intraorbital nesting on the γ_1 band with dominant d_{xy} character (see Fig. 1). For $x \sim 6\%$, in Fig. 5(b) the static susceptibility is much stronger and dominated by the $(\pi,0)$ nesting in the intraorbital channel of the $d_{xz/yz}$-dominated β band. Note that it is also evident from Fig. 5 that the real part of the susceptibility $\chi'(\vec{q},\omega)$ does not have any significant weight around the small $\vec{q}$ regions and is dominated by $\vec{q}$ corresponding to the AFM state. This is unlike the imaginary part of the bare susceptibility $\chi''(\vec{q},\omega)$ that is dominated by the FM fluctuations close to $\vec{q} = 0$. Since the imaginary part of RPA susceptibility is of the form $\chi''(\vec{q},\omega)/\{[1 - U\chi'(\vec{q},\omega)]^2 + [U\chi''(\vec{q},\omega)]^2\}$, for smaller (larger) electron correlations the FM (AFM) fluctuations will dominate. This explains why low-energy FM spin fluctuations are smaller in the dynamical susceptibility shown in Fig. 2 for larger electron correlations.

We now turn to the external Zeeman field along the c-axis direction to study its effect on the longitudinal spin fluctuations in the undoped compound. We aim to study here the high-temperature region where the bare band structure properties dominate the energy scale and nematic fluctuations that are known to be important at low temperatures do not play an important role. Note that for a c-axis magnetic field the Hamiltonian term primarily leads to a shift of the chemical potential for the spin-up and spin-down components. Therefore the effect of the magnetic field on spin susceptibility would be to change the nesting properties of the Fermi surface. In Fig. 6(a), we show variation of the imaginary part of the spin susceptibility with changes in external magnetic field for $x \sim 1\%$ at $\omega = 0.005$. From Fig. 6(a) two effects are apparent. First, we can see from Fig. 6 that an external magnetic field suppresses the spin fluctuations at the AFM wave vector, and for a magnetic field of around $B \sim 0.01$ (in units of hopping t) the AFM and FM fluctuations become comparable in magnitude. Therefore for larger magnetic fields, the material

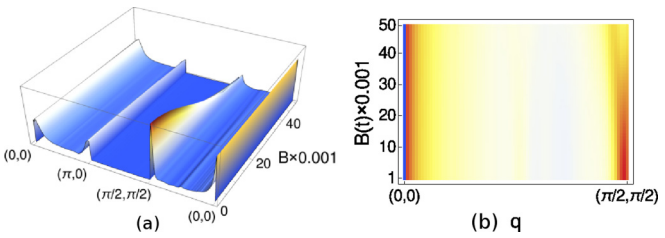

FIG. 6. Dynamical spin fluctuations in the presence of a Zeeman field in Sr327 for $x = 1\%$ doping and $\omega = 0.005$. (a) Three-dimensional plot showing the suppression of AFM fluctuation at $\vec{q} = (\pi/2,\pi/2)$. (b) Two-dimensional plot showing the development of incommensurability in the AFM spin fluctuations for larger magnetic fields.

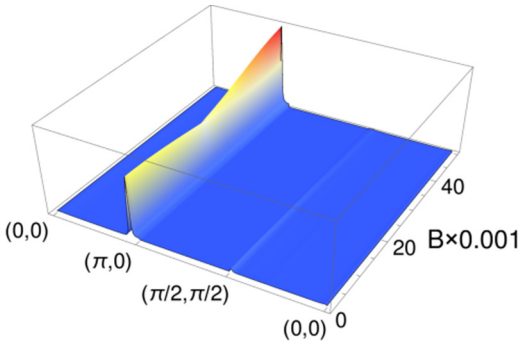

FIG. 7. Dynamical spin fluctuations in the presence of a Zeeman field in Sr327 for $x = 6\%$ doping and $\omega = 0.005$.

properties would be influenced by the stronger competition between the AFM and FM fluctuations. Second, larger external magnetic fields cause the AFM fluctuations to shift from the $\vec{q} = (\pi/2,\pi/2)$ direction. The stronger competition between AFM and FM orders in finite magnetic fields and development of incommensurate spin fluctuations have been observed in neutron scattering experiments [6,25].

These features are, however, not observed in the doped Sr327 compound (see Fig. 7). For a doping of $x \sim 6\%$, the spin fluctuations are not significantly affected by a c-axis Zeeman field; the fluctuations do not become incommensurate like in the undoped compound, and unlike in the undoped compound, the ferromagnetic fluctuations do not compete with the AFM fluctuations at finite magnetic field. As stated earlier, since the spin susceptibility gets suppressed within our model with increasing magnetic fields, it will not lead to a similar SDW instability observed in finite magnetic fields. Therefore additional effects such as nematic fluctuations are likely to play an important role in the development of the SDW instability. It is also useful to note that the change in nesting at the AFM wave vector with small changes in chemical potential brought on by the change in magnetic field leads to a significant effect on the spin susceptibility. An important reason for this effect is the presence of a large density of states due to the presence of a Van Hove singularity on the γ_2 Fermi pockets. Even small changes in chemical potential would therefore lead to a significant change in the density of states at the Fermi energy and therefore a more pronounced dependence of spin susceptibility on magnetic field. In the doped compound the reduced octahedral rotation shifts the Van Hove singularity away from the Fermi energy. This can explain the much weaker dependence of the spin susceptibility on magnetic field strength in doped Sr327, as shown in Fig. 7.

In summary we find that with reduced octahedral rotation and increasing electron doping the spin-fluctuation wave vector in Sr327 shifts from $(\pi/2,\pi/2)$ to $(\pi,0)$ and simultaneously gets enhanced. The enhancement of the spin fluctuations is strong enough to lead to a $\vec{q} = (\pi,0)$ magnetic state as the system approaches the Stoner instability with increasing doping. In the presence of a Zeeman field, we find that the magnetic field suppresses the dominant $(\pi/2,\pi/2)$ spin fluctuations in the undoped compound and leads to a stronger competition between the AFM and FM fluctuations for larger fields. Further the magnetic field also causes the spin fluctuations to become more incommensurate. These observations for the doped Sr327 and in the presence of a Zeeman field are in agreement with neutron scattering experiments.

ACKNOWLEDGMENTS

We are grateful for valuable discussions with P. Aynajian and M. Lawler. This work has been supported by a start-up fund from Binghamton University.

APPENDIX

The on-site interaction Hamiltonian can be generally expressed as

$$H_{\rm INT} = \sum_{i\mu\nu\theta\psi s_1 s_2} U^{\mu\nu s_1}_{\theta\psi s_2} d^\dagger_{i\mu s_1} d_{i\nu s_1} d^\dagger_{i\theta s_2} d_{i\psi s_2}. \tag{A1}$$

Here $U^{\mu\nu s_1}_{\theta\psi s_2}$ is defined using the following symmetries:

$$U^{\mu\nu\uparrow}_{\theta\psi\uparrow} = U^{\mu\nu\downarrow}_{\theta\psi\downarrow} = \bar{U}^{\mu\nu}_{\theta\psi}, \tag{A2}$$

$$U^{\mu\nu\uparrow}_{\theta\psi\downarrow} = U^{\mu\nu\downarrow}_{\theta\psi\uparrow} = \bar{V}^{\mu\nu}_{\theta\psi}. \tag{A3}$$

The $\bar{U},\bar{V}$ tensors are obtained as

$$\bar{U}^{l_3 l_4}_{l_1 l_2} = \begin{cases} \frac{V-J_H}{4}, l_1 = l_2 \neq l_3 = l_4, \\ \frac{J_H-V}{4}, l_1 = l_4 \neq l_3 = l_2. \end{cases} \tag{A4}$$

$$\bar{V}^{l_3 l_4}_{l_1 l_2} = \begin{cases} \frac{U}{2}, l_1 = l_2 = l_3 = l_4, \\ \frac{V}{2}, l_1 = l_2 \neq l_3 = l_4, \\ \frac{J_H}{2}, l_1 = l_3 \neq l_2 = l_4, \\ \frac{J_H}{2}, l_1 = l_4 \neq l_3 = l_2. \end{cases} \tag{A5}$$

The interaction matrix is taken in a spherical approximation which leads to the relation $U = V + 2J_H$. The longitudinal and transverse susceptibilities can be derived following the discussion in Ref. [24]. The expressions for the susceptibilities are

$$\begin{aligned} \hat{\chi}^{zz}_{RPA}(\vec{q},i\omega_n) &= \hat{\chi}^1 + \hat{\chi}^4 - \hat{\chi}^2 - \hat{\chi}^3, \\ \hat{\chi}^{\pm}_{RPA}(\vec{q},i\omega_n) &= \hat{\chi}^5. \end{aligned} \tag{A6}$$

The Dyson equations that define $\hat{\chi}^{1\to 6}$ have been provided in Ref. [24]. After some algebra the final form of the longitudinal spin susceptibility within RPA is a 36×36 matrix given by

$$\begin{aligned} &\hat{\chi}^{zz}_{RPA}(\vec{q},i\omega_n) \\ &= \left[\hat{1} + \hat{M}^{-1}_{22}\hat{M}_{21}\right]\left[\hat{1} - \left(\hat{M}^{-1}_{11}\hat{M}_{12}\right)\left(\hat{M}^{-1}_{22}\hat{M}_{21}\right)\right]^{-1} \\ &\quad \times \hat{M}^{-1}_{11}\hat{\chi}^{\uparrow\uparrow}(\vec{q},i\omega_n) + \left[\hat{1} + \hat{M}^{-1}_{11}\hat{M}_{12}\right] \\ &\quad + \left[\hat{1} - \left(\hat{M}^{-1}_{22}\hat{M}_{21}\right)\left(\hat{M}^{-1}_{11}\hat{M}_{12}\right)\right]^{-1}\hat{M}^{-1}_{22}\hat{\chi}^{\downarrow\downarrow}(\vec{q},i\omega_n), \end{aligned} \tag{A7}$$

$$\hat{M} = \begin{pmatrix} \hat{1} + 4\hat{\chi}^{\uparrow\uparrow}(\vec{q},i\omega_n)\hat{U} & 2\hat{\chi}^{\uparrow\uparrow}(\vec{q},i\omega_n)\hat{V} \\ 2\hat{\chi}^{\downarrow\downarrow}(\vec{q},i\omega_n)\hat{V} & \hat{1} + 4\hat{\chi}^{\downarrow\downarrow}(\vec{q},i\omega_n)\hat{U} \end{pmatrix}, \tag{A8}$$

and the transverse susceptibility within RPA is given by

$$\hat{\chi}^{\pm}_{RPA}(\vec{q},i\omega_n) = [\hat{1} + \chi^{\uparrow\downarrow}(\vec{q},i\omega_n)(4\hat{U} - 2\hat{V})]^{-1}\chi^{\uparrow\downarrow}(\vec{q},i\omega_n). \tag{A9}$$

In the above equations the basis for characteristic wave vector $\vec{q}$ depends on the choice of basis for the tight-binding Hamiltonian. In this study we have worked in the octahedral basis corresponding to the smaller Brillouin zone in Fig. 1(b). One simple check for the above equations would be to look at the limit of the Hubbard model where the electron correlations only contribute to a dominant intraorbital Coulomb term ($l_1 = l_2 = l_3 = l_4$). This significantly simplifies the above equations and leads to exactly the same expressions for longitudinal and transverse susceptibilities derived by Eremin *et al.* [23] to study the single layer Sr_2RuO_4.

[1] S. N. Ruddlesden and P. Popper, Acta Crystallogr. **11**, 54 (1958).

[2] Y. Maeno, H. Hashimoto, K. Yoshida, S. Nishizaki, T. Fujita, J. Bednorz, and F. Lichtenberg, Nature (London) **372**, 532 (1994).

[3] R. S. Perry, L. M. Galvin, S. A. Grigera, L. Capogna, A. J. Schofield, A. P. Mackenzie, M. Chiao, S. R. Julian, S. I. Ikeda, S. Nakatsuji, Y. Maeno, and C. Pfleiderer, Phys. Rev. Lett. **86**, 2661 (2001).

[4] S. Grigera, R. Perry, A. Schofield, M. Chiao, S. Julian, G. Lonzarich, S. Ikeda, Y. Maeno, A. Millis, and A. Mackenzie, Science **294**, 329 (2001).

[5] S.-I. Ikeda, Y. Maeno, S. Nakatsuji, M. Kosaka, and Y. Uwatoko, Phys. Rev. B **62**, R6089 (2000).

[6] C. Lester, S. Ramos, R. Perry, T. Croft, R. Bewley, T. Guidi, P. Manuel, D. Khalyavin, E. Forgan, and S. Hayden, Nat. Mater. **14**, 373 (2015).

[7] J. A. N. Bruin, R. A. Borzi, S. A. Grigera, A. W. Rost, R. S. Perry, and A. P. Mackenzie, Phys. Rev. B **87**, 161106 (2013).

[8] R. Mathieu, A. Asamitsu, Y. Kaneko, J. P. He, X. Z. Yu, R. Kumai, Y. Onose, N. Takeshita, T. Arima, H. Takagi, and Y. Tokura, Phys. Rev. B **72**, 092404 (2005).

[9] M. Hossain, I. Zegkinoglou, Y.-D. Chuang, J. Geck, B. Bohnenbuck, A. C. Gonzalez, H.-H. Wu, C. Schüßler-Langeheine, D. Hawthorn, J. Denlinger *et al.*, Sci. Rep. **3**, 161106 (2013).

[10] M. A. Hossain, Z. Hu, M. W. Haverkort, T. Burnus, C. F. Chang, S. Klein, J. D. Denlinger, H.-J. Lin, C. T. Chen, R. Mathieu, Y. Kaneko, Y. Tokura, S. Satow, Y. Yoshida, H. Takagi, A. Tanaka, I. S. Elfimov, G. A. Sawatzky, L. H. Tjeng, and A. Damascelli, Phys. Rev. Lett. **101**, 016404 (2008).

[11] P. Steffens, J. Farrell, S. Price, A. P. Mackenzie, Y. Sidis, K. Schmalzl, and M. Braden, Phys. Rev. B **79**, 054422 (2009).

[12] J. Hooper, M. H. Fang, M. Zhou, D. Fobes, N. Dang, Z. Q. Mao, C. M. Feng, Z. A. Xu, M. H. Yu, C. J. O'Connor, G. J. Xu, N. Andersen, and M. Salamon, Phys. Rev. B **75**, 060403 (2007).

[13] L. Capogna, E. M. Forgan, S. M. Hayden, A. Wildes, J. A. Duffy, A. P. Mackenzie, R. S. Perry, S. Ikeda, Y. Maeno, and S. P. Brown, Phys. Rev. B **67**, 012504 (2003).

[14] D. J. Singh and I. I. Mazin, Phys. Rev. B **63**, 165101 (2001).

[15] D. Mesa, F. Ye, S. Chi, J. A. Fernandez-Baca, W. Tian, B. Hu, R. Jin, E. W. Plummer, and J. Zhang, Phys. Rev. B **85**, 180410 (2012).

[16] Q. Huang, J. W. Lynn, R. W. Erwin, J. Jarupatrakorn, and R. J. Cava, Phys. Rev. B **58**, 8515 (1998).

[17] A. Tamai, M. Allan, J. Mercure, W. Meevasana, R. Dunkel, D. Lu, R. Perry, A. Mackenzie, D. J. Singh, Z.-X. Shen, and F. Baumberger, Phys. Rev. Lett. **101**, 026407 (2008).

[18] B. Hu, G. T. McCandless, V. O. Garlea, S. Stadler, Y. Xiong, J. Y. Chan, E. W. Plummer, and R. Jin, Phys. Rev. B **84**, 174411 (2011).

[19] G. Li, Q. Li, M. Pan, B. Hu, C. Chen, J. Teng, Z. Diao, J. Zhang, R. Jin, and E. Plummer, Sci. Rep. **3**, 2882 (2013).

[20] C. M. Puetter, J. G. Rau, and H.-Y. Kee, Phys. Rev. B **81**, 081105 (2010).

[21] W.-C. Lee and C. Wu, Chin. Phys. Lett. **33**, 037201 (2016).

[22] W.-C. Lee, D. P. Arovas, and C. Wu, Phys. Rev. B **81**, 184403 (2010).

[23] I. Eremin, D. Manske, and K. H. Bennemann, Phys. Rev. B **65**, 220502 (2002).

[24] X. Wu, F. Yang, C. Le, H. Fan, and J. Hu, Phys. Rev. B **92**, 104511 (2015).

[25] S. Ramos, E. Forgan, C. Bowell, S. Hayden, A. Schofield, A. Wildes, E. Yelland, S. Brown, M. Laver, R. Perry *et al.*, Phys. B (Amsterdam, Neth.) **403**, 1270 (2008).